NTNU – Trondheim
Norwegian University of
Science and Technology

TEM of Chromium doped Zinc Sulfide Thin Films for Solar Cell Applications.

Joakim Larsen

Master of Science in Physics and Mathematics
Submission date: June 2015
Supervisor: Randi Holmestad, IFY
Co-supervisor: Turid Worren Reenaas, IFY

Norwegian University of Science and Technology
Department of Physics

Abstract

Two Cr doped ZnS thin films grown at different temperatures have been studied with transmission electron microscopy. The crystal structure of the films was investigated with high resolution imaging and diffraction patterns. Both samples are highly textured in the [111]-direction of zinc blende, but consist of very small grains with slight deviations in orientation, typically less than 1-2 degrees. The deviations are greater in the sample grown at higher temperature. The sample grown at higher temperature was studied in greater detail, and fast fourier transform analysis of high resolution images along with diffraction patterns showed that it consists of predominantly zinc blende, with a mix of wurtzite and two different polytypes.

The chromium content was investigated by energy-dispersive X-ray spectroscopy and electron energy-loss spectroscopy. The chromium content was determined by energy-dispersive X-ray spectroscopy to be $4.00\% \pm 0.20\%$ in the sample grown at lower temperature, and $6.66\% \pm 1.00\%$ in the sample grown at higher temperature. The distribution of Cr was studied for the sample grown at higher temperature. Both energy-dispersive X-ray spectroscopy and electron energy-loss spectroscopy show that there is Cr throughout the film, but that it is inhomogeneously distributed. A correlation is seen between Cr content and Zn content. In areas with higher Cr content, the Zn content is lower, and vice versa.

ZnS:Cr is a good candidate to realize the concept of intermediate band solar cells. However, the films study here show too many features which would reduce the efficiency of a solar cell. The films need to be further developed to achieve the high efficiency possible with intermediate band solar cells.

Sammendrag

To Cr dopede ZnS tynnfilmer grodd ved forskjellig temperatur har blitt undersøkt med transmisjons elektronmikroskopi. Krystallstrukturen til filmene ble undersøkt med høyoppløsningsbilder og diffraksjonsmønstre. Begge prøvene er sterkt teksturerte i [111]-retningen i zinc blende, men består av veldig små korn med små avvik i orientering, typisk mindre enn 1-2 grader. Avvikene er større i prøven som er grodd ved høyere temperatur. Prøven som er grodd ved høyere temperatur ble undersøkt grundigere, og fast fourier transform ble brukt for å analysere høyoppløsningsbilder. Dette, sammen med diffraksjonsmønstre, viste at strukturen hovedsakelig er zinc blende, med en blanding av wurtzite og to forskjellige polytyper.

Krominnholdet ble undersøkt med røntgenspektroskopi og elektron energitap spektroskopi. Krominnholdet ble funnet av røntgenspektroskopi å være $4.00\% \pm 0.02\%$ i prøven som var grodd ved lavere temperatur, og $6.66\% \pm 1.00\%$ i prøven grodd ved høyere temperatur. Både røntgenspektroskopi og elektron energitap spektroskopi viser at krom er tilstede i hele filmen, men at det er inhomogent fordelt. Det ble funnet en sammenheng mellom kromkonsentrasjon og sinkkonsentrasjon. I områder der kromkonsentrasjonen var høyere, var sinkkonsentrasjonen lavere, og omvendt.

ZnS:Cr er en god kandidat for å få gjennomført mellombånds solceller. Dog viser filmene i dette studiet for mange defekter som vil redusere effektiviteten til en eventuell solcelle. Filmene trenger å bli videreutviklet for å oppnå den høye effektiviteten som er mulig med mellombånd solceller.

Preface

This thesis is the result of my studies during the last semester of my master's degree in applied physics. The project was carried out in the spring of 2015 at the department of physics at the Norwegian University of Science and Technology(NTNU).

I would like to thank my supervisor Randi Holmestad for supervision and guidance. I would also like to thank Turid Worren Reenaas and Mohammadreza Nematollahi for providing the samples I have studied. Finally, I would like to thank Per Erik Vullum, Ragnhild Sæterli and Bjørn Gunnar Soleim for training and assistance in sample preparation and TEM use.

A special thanks goes out to my fiance, Sanna, and my friends and family for moral support.

Trondheim, June 26, 2015

Joakim Larsen

Contents

Chapter 1

Introduction

Global warming has been a hot topic the last decade, and the consensus in the scientific community is that it is caused by human activity [13]. The long term effects of global warming are severe [2], so actions should be taken to stop the current trend. The largest contributor is the release of CO_2 through burning of fossil fuels [1]. The ever increasing demand for energy will cause the amount of fossil fuels burned to increase even further unless we find other, cleaner energy sources. Furthermore, fossil fuels are not renewable and will eventually be depleted. Thus we need to find new energy sources even if we do not take the environment into consideration.

These new energy sources should be renewable, reliable, and safe - both for humans and the environment. The sun fits all these requirements. Each hour, the earth receives more energy from the sun than is consumed in an entire year [11]. With such an abundance of energy, one might think that the energy problem is solved. However, extracting energy from the sun and making it accessible is not a trivial task. Solar cells need to be more financially viable to compete with the relatively cheap fossil fuels. This means that the efficiency has to be increased and/or cost reduced. There are several new concepts for solar

cells which try to accomplish this. One such concept, and what this study will focus on, is the *intermediate band solar cell* which has the potential to outperform conventional solar cells [8].

The project

Chromium doped zinc sulfide (Cr:ZnS) is a good candidate for intermediate band solar cells. ZnS has a wide band gap, and is well known from applications like light emitting diodes and laser diodes. Zinc and sulfur are also abundant and non-toxic, which are important properties for clean energy sources. The ZnS is deposited on a Si substrate as a thin film, and understanding the properties of this film is crucial for improving the technology.

The microscopic structure of a solar cell has a large impact on the macroscopic efficiency of the cell. Every defect will reduce the overall efficiency of the cell. In this study, two Cr doped ZnS thin films that were grown at different temperatures were studied. Mohammadreza Nematollahi, whom grew the films, was unable to give an exact growth temperature other than that one of the samples was grown at a higher temperature than the other. The crystallinity and chromium content, as well as chromium distribution was studied in the two samples. This has been done using transmission electron microscopy (TEM).

Chapter 2 presents some theory on solar cells and how intermediate band solar cells can achieve a higher efficiency than conventional cells. The theory behind TEM is also presented. Chapter 3 presents the experimental work that has been conducted, while chapter 4 presents the results. The results are discussed in chapter 5, and a conclusion is made in chapter 6. Chapter 7 gives some suggestions to what the next steps can be.

Chapter 2

Theory

2.1 Solar Cells

Solar cells are divided into three generations. Conventional solar cells are of the first generation, and consist of single junction (Section 2.1) cells made from high quality crystalline silicon. The production costs of these cells are high, because of the need for high purity silicon. They are still the most financially viable cells because of their price per kWh. The second generation cells use the same principles as first generation, but with a lower production cost. This is done by reducing the material needed to produce a cell. Thin-film technologies and polymers both allow cells to be made thinner. Second generation thin-film cells are typically made of amorphous silicon, CIGS or CdTe. Unfortunately, second generation cells do not have as high efficiency as the high purity silicon cells. Third generation cells use new concepts in an attempt to get a substantially higher efficiency than the first and second generation cells. Some of these concepts are hot-carrier cells, which aim to utilize energy from electrons before thermal relaxation; multiple-carrier cells, with more than one electron-hole pair per absorbed photon; multiple band gap cells, which combines junctions with different band

gaps; and intermediate band solar cells, with an energy band in the band gap. The concept of intermediate band gap cells are detailed in section 2.1. These third generation cells can be constructed from several different materials, and figuring out which materials are best suited for these concepts is the subject of ongoing research.

Pn-junctions and the Photovoltaic effect.

All solar cells rely on the same basic concept; the *photovoltaic effect*. When a photon hits a semiconductor, it can be absorbed and excite an electron from the valence band to the conduction band if the photon's energy is greater than the semiconductor's band gap. This creates two free charge carriers; a hole in the valence band and an electron in the conduction band.

In an unmodified semiconductor, the electron and the hole would recombine without doing any useful work. At the heart of any solar cell is the *pn-junction*, which separates the electron and the hole created by the photovoltaic effect. The name pn-junction comes naturally from the design, shown in Figure 2.1. It is a junction between a P-type and an N-type semiconductor. A P-type semiconductor is a semiconductor doped with an element which has one less electron in the outer shell, for example boron if the semiconductor is silicon. This element is called an acceptor, as it can accept an extra electron from the semiconductor. This lowers the total number of electrons (ie. increases the number of holes) in the semiconductor, bringing the Fermi-level closer to the valence band than in the intrinsic semiconductor. N-type is in many ways the opposite. A semiconductor is doped with an element that has one more electron in the outer shell. This element is called a donor, as it donates an electron to the lattice. The increase in electrons brings the Fermi-level closer to the conduction band [17].

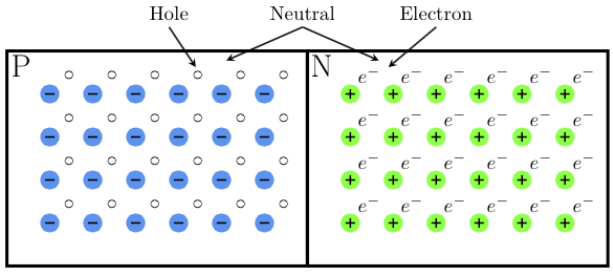

Figure 2.1: A pn-junction before diffusion of mobile charge carriers. Acceptor atoms and holes on the left side, donor atoms and electrons on the right side. There is an equal amount of acceptor atoms and holes, as well as an equal amount of donor atoms and electrons. This makes the net charge zero, so that both regions are neutral.[1]

When a P-type and an N-type semiconductor are brought together to form a pn-junction, the majority charge carriers (electrons for N-type, and holes for P-type) will diffuse over to the other side because of the concentration gradient across the junction. This creates charged regions on both sides of the junction. Positive on the N-side and negative on the P-side. This will continue until the electric field from the charged regions balance the concentration gradient. The area close to the junction is now devoid of any free charge carriers, and is called the *depletion region*. When an electron-hole pair is created via the photovoltaic effect in the depletion region, or within the diffusion lengths of electrons and holes, L_e and L_h respectively, the electron and the hole is separated because of this electric field. This is the driving force in the solar cell [12], and is illustrated in Figure 2.2.

If one considers the whole pn-junction, the Fermi-level must be the same on the P-side and the N-side [17]. This causes the energy bands of the P- and N-type semiconductors to bend across the pn-junction. This corresponds to the electric field mentioned previously. A band diagram for a pn-junction is shown

[1] Figure taken from Eivind Seim's masters thesis. [14]

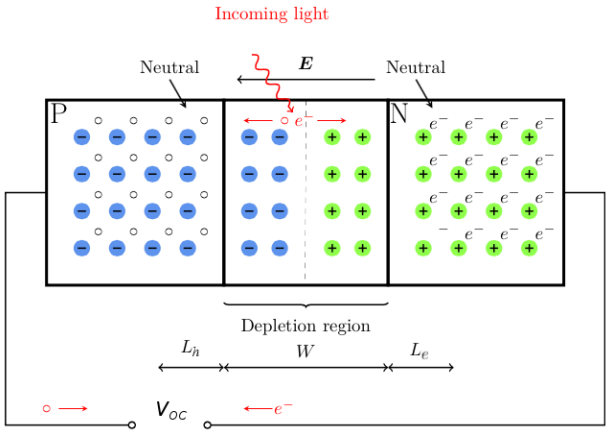

Figure 2.2: Pn-junction with depletion region W. Electron and hole diffusion lengths are indicated with L_e and L_h respectively. (Note that W, L_e and L_h will vary depending on the other factors of the pn-junction.) E indicates the electric field set up by the diffusion of majority carriers. Outside of the depletion region, majority carriers have not diffused and so the net charge is still zero, making these regions neutral. Electron-hole pairs created by absorbed sunlight in the depletion region, or within the diffusion lengths of electrons and holes, are separated and produce a potential, V_{OC}, across the open terminal.[1]

in Figure 2.3.

The current-voltage characteristic of the pn-junction is expressed as

$$I_Q = I_S\left(e^{\frac{eV}{k_B T}} - 1\right) - q\int_{-L_h}^{L_e} \Delta G_e dx \tag{2.1}$$

Where I_S is the reverse saturation current, V is the voltage across the pn-junction, k_B is Boltzmann's constant, T is the temperature, q is the elementary charge, and ΔG_e is the number of electron hole pairs generated per second within W or within a diffusion length from W across an infinitesimal distance dx. [12].

[1] Figure taken from Eivind Seim's masters thesis. [14]

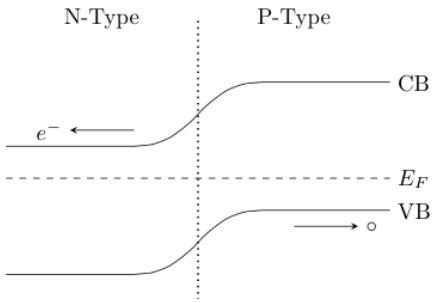

Figure 2.3: Band diagram of a pn-junction showing band bending in the valence band (VB) and the conduction band (CB). E_f indicates the Fermi-level, and e^- and ∘ represents electrons and holes, respectively. While electrons "fall down" to the lowest available energy, holes can be considered as "floating up" to highest available energy [17]. Thus, electron-hole pairs generated in the pn-junction are separated.[1]

Efficiency

Two very important properties of a solar cell is the *open circuit voltage*, V_{OC}, and the *short circuit current*, I_{SC}. The open circuit voltage is the voltage across the open terminal in Figure 2.2, and the short circuit current is the current one would get by short circuiting said terminal. They are given by

$$V_{OC} = \frac{k_B T}{q} \ln\left(1 - \frac{I_{SC}}{I_S}\right) \tag{2.2}$$

$$I_{SC} = -q \int_{-L_h}^{L_e} \Delta G_e dx \tag{2.3}$$

As seen in Equation 2.2, I_{SC} and V_{OC} are not independent of each other. This gives rise to an *IV-curve*, shown in Figure 2.4. This is important for the efficiency, η, of the solar cell. To maximize the efficiency of a solar cell, one needs to maximize the power output of the cell. Electrical power, P, is given by the product $P = VI$, so this is the equation which needs to be maximized. This can be done

[1] Figure taken from Eivind Seim's masters thesis. [14]

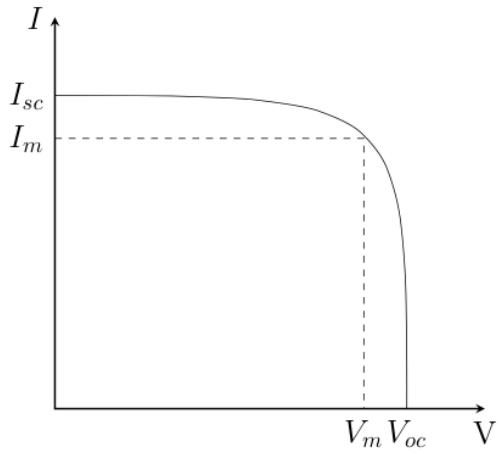

Figure 2.4: Current-voltage curve of a solar cell. Maximizing the area under the curve maximizes the efficiency of the solar cell. This gives the maximum power point, P_m, when $I = I_m$ and $V = V_m$. Figure inspired by Nelson's "The physics of solar cells" [12].

by maximizing the area under the IV-curve. The current and voltage which leads to the highest power output are denoted I_m and V_m, respectively, and give what is called the maximum power point

$$P_m = I_m V_m \tag{2.4}$$

The efficiency, η, tells us how much of the power incident on the cell, P_{inc}, that is converted to electrical power. It is defined as

$$\eta = \frac{P_m}{P_{inc}} = FF\frac{I_{SC}V_{OC}}{P_{inc}} \tag{2.5}$$

Where $FF = \frac{P_m}{I_{SC}V_{OC}}$ is the *fill factor*. The fill factor is often used to compare solar cells, along with I_{SC} and V_{OC}.

Limitations

Equation 2.5 can give very high theoretical efficiencies for ideal solar cells. The true efficiency of the cells, however, is nowhere near the theoretical maximum. To be able to create better solar cells, it is important to understand what limits the efficiency of a cell. Some factors are easy to deduce, while potentially impractical to counter, especially in certain situations. These are effects like dust/snow gathering on the cell, shadows from the surrounding area, clouds, and light reflected from the cell. Other factors might require more knowledge, like the physical properties of the solar cell and the sun's radiation spectrum.

Recombination

Defects in the crystal structure of the semiconductor increase the chance of *recombination*. Recombination is the opposite of electron-hole pair generation, and is when an electron falls down from the conduction band to fill a hole in the valence band. The energy is then released as a photon, phonon or both. When considering efficiency, there are two types of recombination; *radiative* and *non-radiative*.

Radiative recombination is recombination that releases a photon. This photon can be reabsorbed in the solar cell and excite a new electron-hole pair. Photons released by recombination do not reduce the efficiency unless they escape the cell.

Non-radiative recombination release the energy as a phonon. This can happen directly, or through *Auger recombination*. In Auger recombination, the energy is used to excite an electron that's already in the conduction band. This Auger electron releases the extra energy as phonons through thermal relaxation. Auger recombination is unavoidable, and is closely linked to doping levels [12].

Shockley-Read-Hall-recombination (SRH-recombination) is the most impor-

tant recombination mechanism in real semiconductors. It is also called *impurity recombination*, because it comes from impurities in the crystal lattice. Lattice defects can introduce *impurity states* in the semiconductor [12]. These impurity states are available states in the band gap. Impurity states, especially those close to the middle of the band gap, increase recombination rate and are often called recombination centers [17]. The recombination caused by SRH-recombination is mostly non-radiative. Even if the recombination is radiative, the excited photon will not have enough energy to create a new electron-hole pair, and is thus still an energy loss.

Spectrum losses

While not a loss per se, *spectrum losses* refer to the fact that not all the energy in sunlight can be extracted by a single cell. Photons with an energy lower than the band gap can not create an electron-hole pair, and does not contribute to the current. The energy gap of silicon is 1.1 eV. 19% of the solar spectrum is below this energy [6], which severely limits the energy that can be gained from solar radiation. In addition to that, photons with energy greater than the band gap will not contribute all their energy to the current. The energy exceeding the band gap will be lost through thermal relaxation of the electrons. Thus all absorbed photons will only contribute an energy equal to the band gap of the solar cell. Spectrum losses limit the efficiency of a perfect single junction cell with an optimal band gap to 33.7%[1] [15].

Intermediate band solar cells

Intermediate band solar cells is a third generation concept which tries to combat spectrum losses. This is done by introducing a narrow energy band within the

[1] There are several ways of calculating efficiency, using different air masses and different light concentration. This number used an air mass of 1.5 and radiation equal to 1 sun.

band gap of a semiconductor. The purpose of this is to have more than one energy level available for absorption. This is the same concept that multi-junction cells use. The advantage of intermediate band cells is that while multi-junction cells require several cells to be placed on top of each other, making it technologically difficult and requiring a lot of material, the intermediate band cell only requires one extra layer of material compared to single junction cells. Intermediate band cells are therefore much cheaper than multi-junction cells.

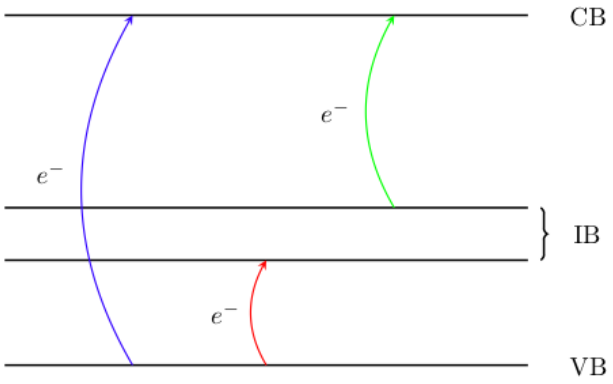

Figure 2.5: Energy band of an intermediate band material. There are three different energy gaps available for absorption, allowing lower energy photons to be absorbed at the same time as high energy photons can contribute more of their energy.[1]

An illustration of the intermediate band and the different energy gaps can be seen in Figure 2.5. If the lowest energy gap is lower than the energy gap of conventional cells, lower energy photons can contribute to the current. The presence of the larger gaps will at the same time allow higher energy photons to contribute more of their energy. The goal is to increase the number of photons that contribute to the current while at the same time increasing the energy that high-energy photons can contribute. The theoretically ideal band gap for an in-

[1] Figure taken from Eivind Seim's masters thesis. [14]

termediate band solar cell with one intermediate band is 1.95 eV with additional gaps of 0.71 eV and 1.24 eV introduced by the intermediate band [10]. An important consideration is that the flow of electrons from the valence band to the intermediate band must be equal to the flow from the intermediate band to the conduction band. This is because a partially filled intermediate band is needed to allow for three different absorption energies. The intermediate band material is inserted within the depletion region of a normal pn-junction, between the p-side and the n-side, and apart from the intermediate band, the cell operates the same way as a conventional cell.

There are three ways to introduce such an intermediate band [10]: highly mismatched alloys, quantum dots and ultrahigh doping. The most developed technique is quantum dots, which have reached an efficiency of 18.7%[1] [19]. Many of the intermediate band solar cell designs rely on scarce or toxic materials, such as GaAs, which is not compliant with a cheap and safe energy alternative. An exception to this is zinc sulfide with ultrahigh chromium doping. The chromium creates an intermediate band within the band gap of ZnS. Normally, impurities create recombination centers which reduce the efficiency of a solar cell. It has, however, been shown for Ti doped Si that ultrahigh doping introduce less SRH-recombination than moderate doping levels [9].

2.2 Transmission Electron Microscopy

All information in this section is taken from the book "Transmission Electron Microscopy, Part 1: Basics" by David Williams and Barry Carter [20], unless specified otherwise.

In a transmission electron microscope (TEM), an electron beam is transmitted through a specimen. The beam interacts with the specimen when it passes

[1] Air Mass 1.5 and 1 sun.

through, and these interactions allow us to form images of the specimen. It is similar to a visual light microscope, with three major differences: Electrons are used instead of photons, the electrons are transmitted through the specimen instead of reflected, and the refractive lenses are replaced by magnetic lenses. There are many signals that can be analyzed when an electron beam hits a specimen (and an array of different techniques to do so). This section will only consider those which are relevant for this study: Unscattered electrons, which pass through the specimen without interacting; elastically scattered electrons, which are scattered by the specimen without losing energy; inelastically scattered electrons, which lose energy as they pass through the specimen; and characteristic x-rays caused by electron excitation and relaxation.

Why use electrons?

For a visual light microscope, the smallest resolvable distance, δ, is given by the Rayleigh criterion

$$\delta = \frac{0.61\lambda}{\mu \sin\beta} \tag{2.6}$$

where λ is the wavelength of the photons, μ is the refractive index of the viewing medium, and β is the collection semi-angle of the magnifying lens. In an ideal situation using blue light one gets a maximum lateral resolution of 200 nm. The lattice spacing in Si is 0.543 nm [7], so it is obvious that a visual light microscope is no good to observe these structures. The relativistic de Broglie wavelength of an electron is given by

$$\lambda = \frac{h}{\sqrt{2m_e E_k \left(1 + \frac{E_k}{2m_e c^2}\right)}} \tag{2.7}$$

where h is the Planck constant, m_e is the mass of the electron, E_k is the electron's kinetic energy, and c is the speed of light. With an acceleration voltage of 200 kV, which is used in this study, the wavelength becomes 0.00251 nm. This is much

smaller than the radius of an atom (~0.1 nm), making it theoretically possible to observe individual atoms. There are however other factors that severely limit the resolution of TEMs, such as the lenses.

The instrument

The formalism from visual light microscopes can be used for TEMs even though they work by different mechanisms. Glass lenses and mirrors are used to focus the beam in visual light microscopes, while a TEM uses electromagnets instead. These electromagnetic lenses are much worse than the lenses in a visual light microscope[1], and severely limit the resolution one can obtain in a TEM. State of the art TEMs have lenses which correct for spherical aberrations, making it possible to image individual atoms. An overview of the instrument with ray diagrams is shown in Figure 2.6. Special notice should be given to the *image plane*; where an image of the specimen is present, ie. where rays that originate from the same place of the specimen converge to a point; *back focal plane*, where rays that exit the specimen at the same angle converge to a point; *objective aperture*, which is an aperture in the back focal plane that allows beams scattered to certain angles to be selected for imaging; and the *selected area diffraction(SAD) aperture*, which is an aperture in the image plane that lets one isolate a selected area of the specimen for imaging.

Diffraction

Diffraction patterns arise from elastically scattered electrons, and is a widely used technique for studying the crystal structure of solids. The theory behind diffraction was developed for X-rays, but is applicable for electrons when viewed as waves. An in-depth explanation of diffraction can be found in “Introduction

[1] Sometimes compared to using the bottom of a soda bottle as a lens.

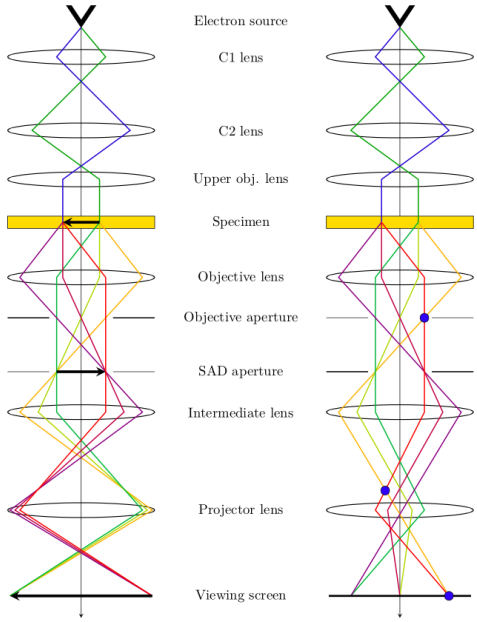

Figure 2.6: Conceptual image of a TEM operating in image mode on the left side, and in diffraction mode on the right side. In image mode, the image plane located at the SAD aperture is magnified and projected on the viewing screen. In diffraction mode, the back focal plane at the objective aperture is projected. Note that real TEMs have more lenses and apertures than in this figure.[1]

to Solid State Physics" by Charles Kittel [7], this section will only include the most relevant points.

When an electron with high kinetic energy hits a crystal, it can interact with atoms in the crystal and can be scattered. The scattering from atom planes with the same orientation can give constructive interference if the path difference is a multiple of the electrons' wavelength. This condition is known as Bragg's law and is given as

$$n\lambda = 2d\sin\theta \tag{2.8}$$

where n is an integer, λ is the wavelength of the electrons, d is the spacing be-

[1] Figure taken from Eivind Seim's masters thesis. [14]

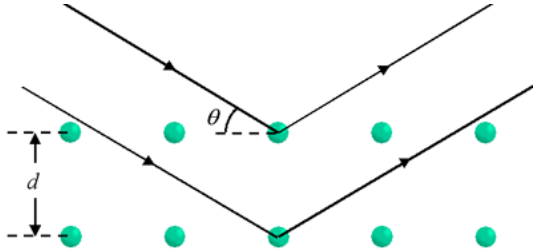

Figure 2.7: Illustration of Bragg's law. d is the distance between atom planes and θ is the scattering angle. The two waves will only have constructive interference if the path distance is a multiple of the electrons' wavelength. Figure inspired by Kittel's "Introduction to solid state physics" [7].

tween atom planes, and θ is the scattering angle. An illustration of this is given in Figure 2.7.

Because diffraction is dependent on the orientation of the atom planes and the distance between them, it is closely related to the crystal structure of a material. The dependency on the orientation also means that one can use the diffraction pattern to determine if the specimen consists of a single crystal or several crystals with different orientation. The diffraction pattern from a single crystal consists of isolated spots, whereas the pattern from a polycrystalline sample will depend on the number of crystals and their relative orientation. For randomly oriented crystals with sufficiently many crystals, the pattern will look like rings. This is because the different orientations of the grains in the polycrystalline material make the spots appear in different positions in the diffraction pattern. Since the d-spacing of all the grains is the same, all these spots will be at the same distance from the center of the pattern. If the crystals are not randomly oriented, but are distributed around a preferred orientation, the pattern will look like the pattern from a single crystal except that it will be smeared out around the axis of rotation. In the center of a diffraction pattern, one finds the electrons which were not scattered. This is in most cases the spot with highest

(a) Diffraction from a single ZnS crystal.

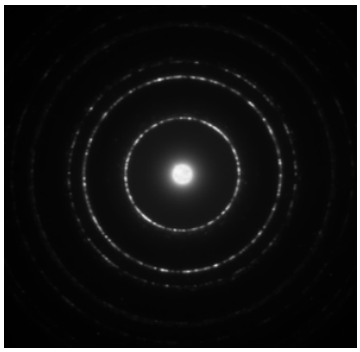

(b) Diffraction from polycrystalline ZnS.

Figure 2.8: Diffraction pattern from a single crystal and from a polycrystalline sample. The single crystal give distinct spots, while the polycrystalline give rings. This is because the distance from the center is dependent on lattice spacing, which is the same for all the grains in the sample, while the angular position depends on the orientation of the individual grains.

intensity. An example of diffraction from a single crystal and a polycrystalline sample is given in figure 2.8a and 2.8b, respectively.

Imaging in TEM

Contrast is the difference in intensity observed in an image. It is easier to distinguish details with higher contrast. Understanding contrast differences is important to interpret TEM images. There are two main types of contrast: Amplitude and phase contrast. Amplitude contrast is divided into mass-thickness contrast and diffraction contrast.

Mass-thickness contrast is caused by incoherent scattering. Heavier elements scatter more than lighter elements, making heavier elements less transparent to electrons. The amount of scattering, and thus transparency, is also dependent on thickness. If the beam passes through more material, there are more possibilities for scattering. The mass-thickness contrast is often called Z-contrast because of

its dependency on atomic number (Z-number).

Diffraction contrast is the most important source of contrast in bright-field and dark-field images. As discussed previously, scattering is dependent on the orientation of the crystal. Grains with different orientation will scatter differently, and a contrast difference is observed.

Phase contrast is contrast caused by phase differences in the electrons. It can be seen as fringes caused by e.g. uneven thickness or stacking faults.

Bright field and dark field imaging

Bright field(BF) and *dark field*(DF) imaging are imaging techniques that take advantage of a specimen's diffraction pattern. The objective aperture is used to select which reflections in the diffraction pattern are used to form the image. In bright field imaging, the center spot in the diffraction image is selected, so that only unscattered electrons are used to form the image. This causes grains that are in Bragg condition to be considerably darker than those that are not. In dark field imaging, the objective aperture is used to select a diffraction spot so that the image is formed by electrons that were scattered to the same angle.

Scanning transmission electron microscopy

Scanning transmission electron microscopy(STEM) is differentiated from regular TEM because of the different working principles. Where regular TEM illuminates the whole specimen at once, STEM focuses the electron beam on a single spot on the specimen which scans across the area of interest. The transmitted beam is detected by dedicated bright field and dark field detectors to form an image of the specimen. The bright field detector resembles a camera in regular TEM. It detects the direct beam and maps the intensity from a spot on the specimen to a pixel in the image. Dark field in STEM differs more from dark field in

TEM. Instead of selecting a single diffraction spot to use for imaging, the detector collects all diffracted electrons between set angles. These angles depend on the *camera length*. The camera length is simply the distance form the specimen to the diffraction pattern in the back focal plane. A longer camera length lets the detector collect electrons scattered to shorter angles, and vice versa.

Spectroscopy

One big advantage of STEM is apparent when doing spectroscopy. In TEM, the spectroscopy signals originate from the whole area of the specimen which is illuminated. Because STEM only illuminates a very small spot and scans across the area of interest, one can map the spectroscopy data to a single spot on the specimen. To name an example, this allows for not only the detection of which elements the specimen consists of, but also where said elements are in the specimen. This study uses two kinds of spectroscopy; *electron energy-loss spectroscopy* and *energy-dispersive X-ray spectroscopy*.

Electron energy-loss spectroscopy

As mentioned earlier, elastically scattered electrons give rise to diffraction patterns which can be utilized in a lot of different techniques to find information about the specimen. Not all scattering events are elastic, however. These inelastic scattering events make the electrons lose some energy, which opens up the possibility of *electron energy-loss spectroscopy* (EELS). EELS is a powerful tool which can give information about e.g. valence state of elements, specimen thickness, atomic composition and dielectric constant.

To filter out the elastically scattered electrons, an aperture is placed in the optical axis. Bragg scattered electrons will hit the aperture and will not contribute to the signal. The beam that passes through the aperture is deflected 90° from

the optical axis in a magnetic tube. Because the Lorentz force is dependent on energy, the electrons will be separated according to how much energy they have lost. A multipole projector lens system makes sure that the electrons are well separated spatially as a function of their energy, and that electrons with the same energy hit the detector at the same place.

Energy-dispersive X-ray sectroscopy

One of the ways electrons lose energy when scattering inelastically is by excitation of a core electron from an atom. If an electron transfers more than a critical amount of energy to a core electron, it will be excited above the Fermi level of the crystal and escape the atom. This ionized atom can return to its lowest energy state by filling the hole with an electron from an outer shell. This is similar to recombination discussed in Section 2.1, but instead of an electron from the conduction band filling a hole in the valence band, we have an electron from an upper shell filling a hole in a lower shell, e.g. an L-shell electron filling a hole in the K shell. The excess energy is released by exciting an Auger electron, or by emitting a photon. Because of the scale of the energy differences between the electron shells, this photon will be an X-ray. The technique of studying these X-rays is called *energy-dispersive X-ray spectroscopy* (EDS)[1]. These X-rays are often called characteristic X-rays. This is because the energy differences between electron shells is dependent on material. Thus the possible energies the X-rays can have give each element its own distinct fingerprint.

There are a lot of similarities between EELS and EDS, since the mechanism that gives rise to an EDS signal is a large part of the EELS signal. There are some differences, however, that separate EELS from EDS. EELS has much better energy resolution, so much that it is possible, with the proper setup, to differentiate

[1] Also shortened EDX or XEDS. Sometimes called energy-dispersive X-ray analysis (EDXA) or energy-dispersive X-ray microanalysis(EDXMA)

which sub-shell an electron was excited from. Having such high energy resolution limits the range of energies which can be detected at the same time, so not all elements can be studied simultaneously with such high energy resolution. EELS is not well suited to study heavy elements because the signal decreases exponentially with energy loss, making the signal from heavy elements weak. EDS has a significantly higher signal to noise ratio, but also has some artefacts which are not present in EELS, such as stray signals and sum peaks. One big practical difference is that EDS is much easier to set up and perform, while EELS takes time and requires an experienced operator.

2.3 The material

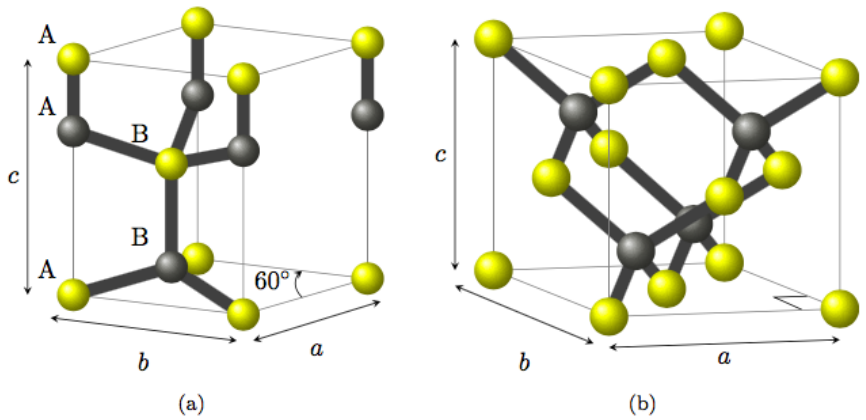

Figure 2.9: (a) shows the hexagonal wurtzite structure of ZnS. (b) shows the FCC zinc blende structure. Yellow spheres represent sulfur atoms, and grey spheres represent zinc atoms. The sulfur atoms in wurtzite form an ABAB stacking sequence in the [001]-direction. Both these structures have a two-atomic basis. Wurtzite has sulfur in (000) and zinc in $\left(00\frac{5}{8}\right)$, while zinc blende has sulfur in (000) and zinc in $\left(\frac{1}{4}\frac{1}{4}\frac{1}{4}\right)$. [1]

[1] Figure taken from Eivind Seim's masters thesis. [14]

Zinc sulfide, ZnS, is used in a wide variety of applications. Some of these are electroluminescent devices, blue and ultraviolet light emitting diodes, and laser diodes. ZnS is a polymorphic material, which means that it can form more than one crystal structure. It is most commonly found with a face-centered cubic (FCC) structure, but can also form a hexagonal close packed structure(hcp) [16]. The structure is shown in Figure 2.9. The zinc blende and wurtzite structure are the most common structures for III-V and II-VI compounds [4]. ZnS has different band gaps in these structures. For intermediate band solar cells, the FCC structure with a band gap of 3.7 eV is most interesting [16].

The FCC structure of ZnS has a two-atomic basis with sulfur in (000) and zinc in $\left(\frac{1}{4}\frac{1}{4}\frac{1}{4}\right)$. This structure is also called zinc blende or sphalerite, referred to as zinc blende from now on, and belongs to the F$\bar{4}$3m space group. The lattice parameter of zinc blende is 5.41 Å [5], which is almost identical to that of Si [14].

The hexagonal structure of ZnS is called wurtzite(and is referred to as such from now on), and belongs to the P6$_3$mc space group. Similar to the zinc blende structure, wurtzite also has two atoms in the basis with sulfur in (000) and zinc in $\left(00\frac{5}{8}\right)$. The lattice constants for wurtzite are $a = b = 3.820$ and $c = 6.260$ [18].

Polytypism

Polytypism is a special case of polymorphism where the structural differences are in a single crystal direction. The wurtzite and zinc blende structures are polytypes. If one considers the S atoms along the [111] direction in zinc blende, they have an ABCABC stacking sequence, where A, B and C denotes different positions projected in the (111) plane. Wurtzite, on the other hand, has an ABABAB stacking sequence along the [001] direction. Note that [111] in zinc blende is equivalent to [001] in wurtzite.

Chapter 3

Experimental work

3.1 Pulsed Laser Deposition

The samples in this study were created by Mohammadreza Nematollahi using *pulsed laser deposition* (PLD). PLD is a technique for deposition of thin films on a substrate. The setup has four main parts: the substrate, which the film will be deposited on; a laser capable of creating very short pulses; the target, which is made of the material you want to deposit; and a ultra-high-vacuum (0.27 nPa) chamber. A schematic view of the setup can be seen in Figure 3.1. The target and substrate are in the ultra-high-vacuum chamber. The laser emits short high powered pulses that hit the target, causing parts of it to evaporate. The evaporated material is in a plasma state and is visible as a plume normal to the target surface. The high energetic ions in the plasma can then travel to the substrate where they can nucleate and create a film.

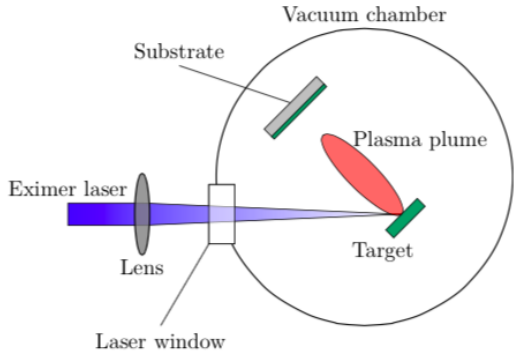

Figure 3.1: Schematic view of a PLD setup. A focused, pulsed laser vaporizes material from the target to a plasma. The ions in the plasma can then travel to the substrate and nucleate to form a film.[1]

3.2 Sample Preparation

The two most obvious factors of a TEM sample is that it fits in the sample holder, and that it is thin enough to be electron transparent. How thin it needs to be depends on beam energy, the average atomic number in the specimen and what features one is trying to observe [20]. For our purposes, the thickness should be in the order of 10-50 nm. There are many ways to prepare a sample for TEM [20]. Which technique to use depends on what kind of sample is to be studied, and what properties that are to be investigated. The samples in this study were made as cross-section samples by dimpling and ion milling, following the procedure developed over time in the TEM Gemini Centre group [14].

First, the sample is fastened, film down, on a glass plate. This is done by heating the glass plate with wax on top to about 125°C on a Framo Gerätetechnik M21 hot plate. The wax then melts, and the sample is placed, film down, on the wax. The glass plate is taken off the hot plate, and left to cool down so the wax hardens. When the sample is secured on the glass plate, two 2 mm x 8 mm strips

[1] Figure taken from Eivind Seim's masters thesis. [14]

are cut with a Testbourne Model 650 Diamond Wheel Saw using a 150 μm thick Allied High Tech Wafering blade.

The strips are placed in an acetone bath to dissolve the leftover wax after the cutting, and then they are placed in an ethanol bath to remove the dissolved hydrocarbons. The strips are left in each bath for about five minutes. The strips are then glued together with Allied High Tech EpoxyBond 110 glue, film to film, making a substrate-film-film-substrate sandwich, as shown in Figure 3.2. Strips of silicon are used as support, and to make the sandwich height closer to the inner diameter of a brass tube it will be inserted in. This is to reduce the amount of glue between the sample and the brass tube as the glue can be a source of contamination, especially during ion milling. The glue hardening and resin parts are mixed in a 1 to 10 ratio, and a small amount is applied to each strip with a wooden toothpick. The sandwich is placed in a clamp, and put on the hot plate for approximately 50 minutes at 100°C to cure the glue.

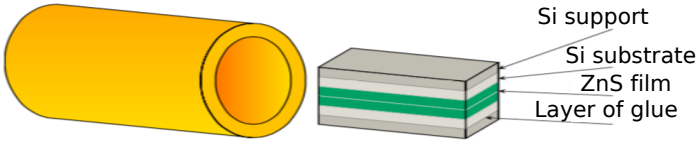

Figure 3.2: Schematic view of the substrate - film - film - substrate sandwich and the brass tube.[1]

When the glue has cured, the sandwich is ground using a Struers RotoPol-21 grinding machine equipped with a SiC Grit P2500 (average particle size 6.5 μm) grinding paper to fit in a hollow brass tube with inner diameter 2 mm (outer diameter 3 mm). While grinding the sandwich, the tube is glued vertically to a small piece of Si. This glue is cured at 150° for 5-10 minutes. When the sandwich fits in the tube, the tube is filled with glue. It is important to avoid air bubbles

[1] Figure taken from Eivind Seim's masters thesis [14]

in the cylinder. The sandwich is then inserted in the tube and once again left on the hot plate to cure at 100°C for 50 minutes.

The cylinder is then placed on the diamond wheel saw, and cut into 1 mm thick discs. The discs are inspected with a visual light microscope. The disc with the least amount of damage is then fastened to a dimpling stub with wax in the same way as the sample was first fastened to the glass plate. The disc is then ground on the RotoPol-21 first with P2500 grinding paper, and then with P4000 (average particle size 2.5 μm) grinding paper until the surface is as smooth as possible. The stub is then heated to approximately 125°C to soften the wax. The disc is then turned upside down and fastened with the now smooth side down, using as little wax as possible. The disc is then ground with P2500 grinding paper until the thickness is approximately 110 μm, and then ground with P4000 grinding paper till the thickness is 80-90 μm. Thickness is measured using a calibrated Olympus BX60 visual-light microscope.

When the disc has a suitable thickness, it is placed(still attached to the dimpling stub) on an EAF Instruments Model 2000 dimpler. The machine grinds out a spherical pit called a dimple in the disc, as shown in figure 3.3. When finished, the thickness of the sample at the bottom of the dimple should be 10-15 μm. The grinding rate is set to 1 μm per minute until the sample is $\sim 30\mu$m and is then set to 0.5 μm per minute until the desired thickness is achieved. 1 μm Allied High Tech Polycrystalline Diamond Compound mixed with distilled water is used as grinding lubrication. When the dimple is finished, the stub is placed in acetone to dissolve the wax holding the specimen. After the specimen is released from the stub, it is left in the acetone for 5 minutes, and is then placed in an ethanol bath for five minutes as before.

The last part of the sample preparation is the ion milling. The Gatan Precision Ion Polishing System Model 691 (PIPS) uses beams of argon ions to sputter away material, to end up with a small hole in the sample. The specimen is placed

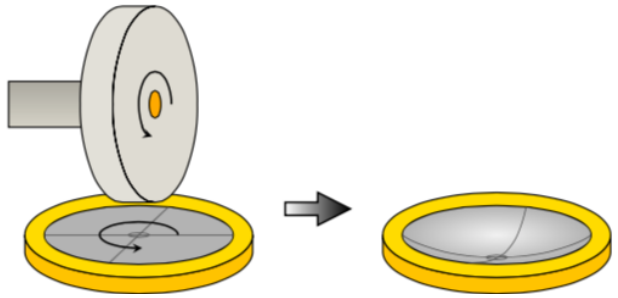

Figure 3.3: A rotating grinding wheel is carefully lowered while the stage is rotating the specimen to make the dimple. A mixture of distilled water and 1 μm Allied High Tech Polycrystalline Diamond Compound paste ensures gentle grinding. The gray lines only illustrate the topology of the sample.[1]

dimple side up in a special PIPS-holder, with the glue layer parallel to the clamps on the holder. It is then lowered into the vacuum chamber in the PIPS. The sample is left for 15 minutes to cool down. The PIPS then uses two beams of argon ions to sputter a hole in the sample. One beam 4°(relative to the surface of the sample) from below, the other one 4° from above. Staring with a beam energy of 4 keV, with the PIPS in double-sector mode. When the silicon substrate becomes orange, the specimen is almost penetrated. When a hole appears, the beam energy is gradually lowered to 1 keV over an hour. Ion milling can damage the crystal structure of the specimen, and leave an amorphous layer. The gradual lowering of beam energy reduces the amorphization effect.

Some of the samples in this study were ion milled using the new Gatan PIPS2. The procedure was almost identical, except for the beam energy. The higher efficiency of the PIPS2 allowed a faster reduction of the ion energy to reduce amorphization. As soon as a hole was detected, the energy was reduced to 2 keV. It was then milled at 2 keV, 1 kev and 0.3 keV for 10 minutes each.

[1] Figure taken from Eivind Seim's masters thesis [14]

3.3 The Microscopes

Two microscopes were used to study the samples. One JEOL 2100 TEM with a LaB_6 electron source, and a Gatan 2k Orius CCD camera. This microscope was used for dark field imaging, high resolution bright field imaging, diffraction and EDS. A double aberration corrected JEOL ARM200F with a cold FEG electron source, operated by Sintef researcher Per Erik Vullum was used for a detailed study of one of the samples by HRTEM, EDS and EELS. The acceleration voltage was 200 keV at all times.

Chapter 4

Results

This chapter presents the results from the two film samples that were studied; one grown at a lower temperature, and one at a higher temperature. High resolution images and diffraction patterns obtained on the JEOL 2100 are presented first, as well as average chromium content for the two samples, followed by high resolution images, EDS and EELS spectra from the JEOL ARM200F. Only one specimen, which came from the sample grown at higher temperature, was studied in the ARM200F. When a crystallographic direction is stated, this refers to the direction in the substrate, which is the same as in zinc blende, unless otherwise specified.

4.1 Crystal structure

High resolution images of the sample grown at lower temperature, and at higher temperature are shown in Figure 4.1 and Figure 4.2, respectively. Atomic (111) planes can be seen in the substrate and throughout the films, indicating that both samples are highly textured in the [111]-direction, which is also the growth direction. Some stacking faults can be seen in both images, but no clear grain

boundaries. The uneven contrast, which is especially noticeable in Figure 4.1, is caused by uneven thickness as a result of specimen damage from the ion milling during sample preparation. Notice also that an amorphous layer can be seen between the substrate and the film. This amorphous layer was observed in all high resolution images, and had a varying thickness from 1 nm to 4 nm. The thickness of this layer was fairly constant over each electron transparent area of a specimen, but varied between different specimen and between separate areas of the same specimen.

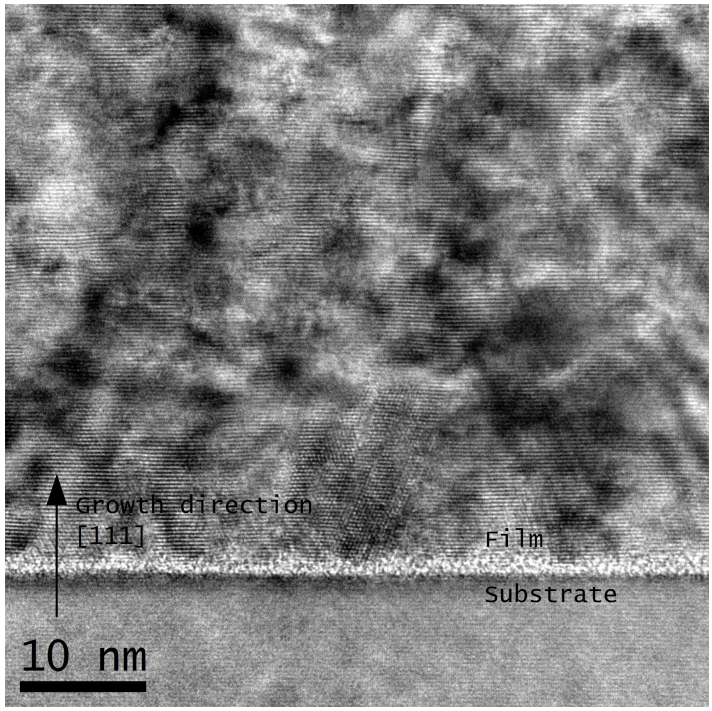

Figure 4.1: High resolution image of the sample grown at lower temperature. Atomic (111) planes can be seen in the substrate and throughout the film. Stacking faults are also seen in the film, most noticeable in the middle close to the substrate. An amorphous layer is noticed between the substrate and the film. This image was taken on the JEOL 2100. The uneven contrast is caused by thickness variations introduced by the ion milling during sample preparation.

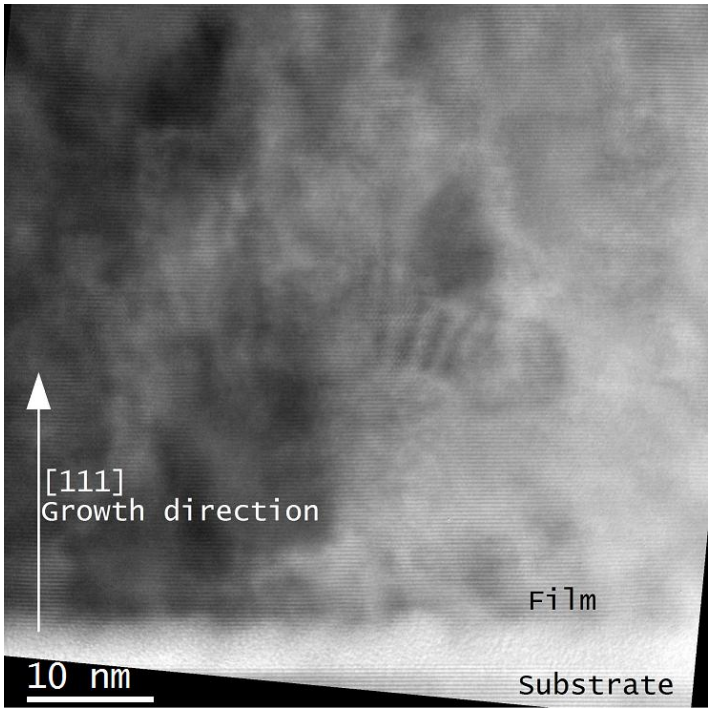

Figure 4.2: High resolution image of the sample grown at higher temperature. Atomic (111) planes can be seen in the substrate and throughout the film. Stacking faults are also seen in the film, most noticeable in the middle where they give rise to Moiré fringes. An amorphous layer is noticed between the substrate and the film. This image was taken on the JEOL 2100.

Diffraction patterns from the sample grown at lower temperature and the sample grown at higher temperature can be seen in Figure 4.3 and Figure 4.4 respectively. These show that both samples are very highly textured, but all reflections except the center spot are smeared out, slightly rotated around the center. This effect is greater for the sample grown at higher temperature. Note that the sharp spots in Figure 4.4 originate from the substrate.

One specimen from the sample grown at lower temperature had a different diffraction pattern than what is observed in Figure 4.3 in one area. This is shown

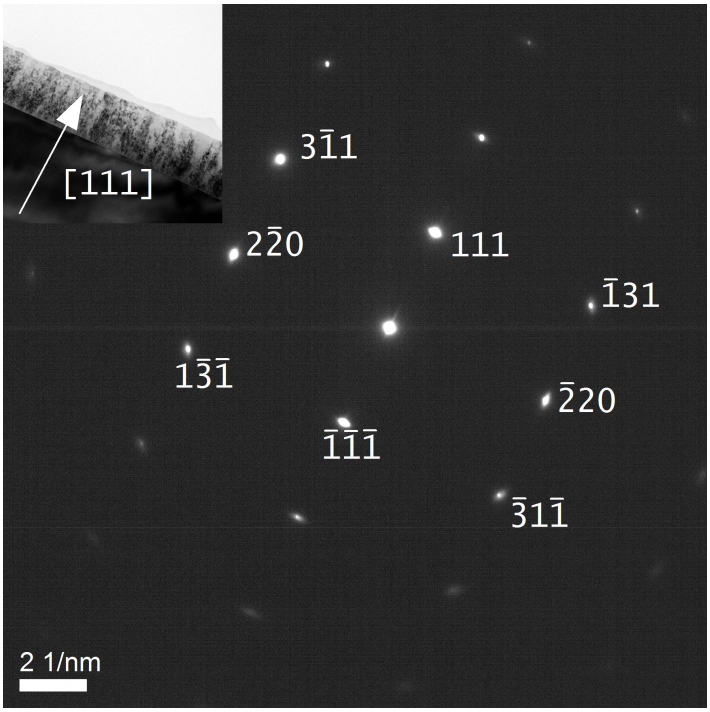

Figure 4.3: Diffraction pattern from the sample grown at lower temperature with the electron beam parallel to the [11$\bar{2}$]-direction. The upper left corner shows the area used to obtain the diffraction pattern. The arrow indicates the [111]-direction, which is also the growth direction. Notice that the reflections are smeared out, slightly rotated around the center spot, indicating that the film is not perfectly monocrystalline, but consists of several grains with almost identical orientation.

in Figure 4.5. Note that this was observed in only one area of this specimen. The other electron transparent parts of the same specimen, and every other diffraction pattern obtained from the sample grown at low temperature (a total of 15 different areas were studied), show a diffraction pattern similar to the one in Figure 4.3. Figure 4.5 shows a diffraction pattern from the substrate's FCC structure, and from a polycrystalline wurtzite structure in the film. The wurtzite structure is textured in the hexagonal [001]-direction, which is the same as the substrate's

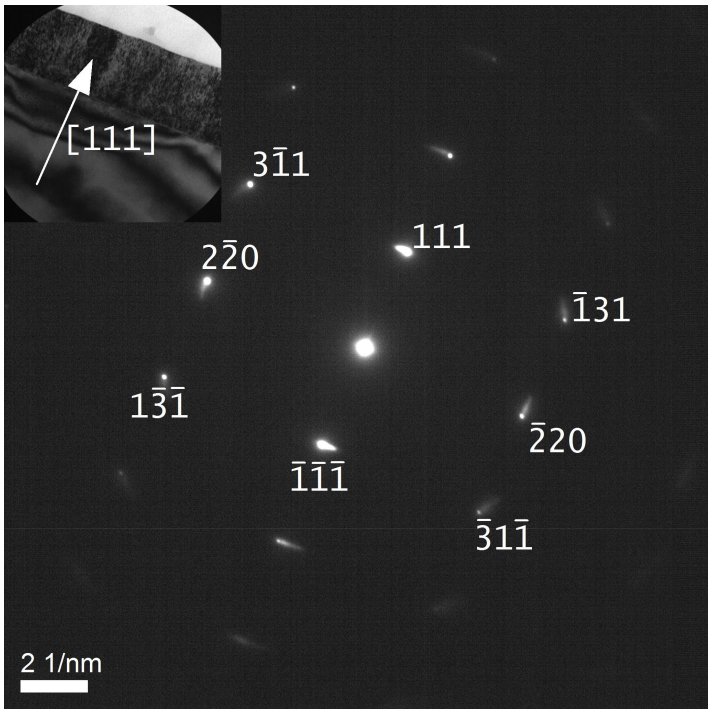

Figure 4.4: Diffraction pattern from the sample grown at higher temperature with the electron beam parallel to the [11$\bar{2}$]-direction. The upper left corner shows the area used to obtain the diffraction pattern. The arrow indicates the [111]-direction, which is also the growth direction. Notice that the reflections are smeared out, slightly rotated around the center spot, even more so than in Figure 4.3. The sharp spots in each reflection originate from the substrate.

[111]-direction, and is also the growth direction. However, the structure is less textured than that observed in Figure 4.3 and Figure 4.4.

The specimens discussed up until this point were prepared so that the electron beam entered along the [11$\bar{2}$]-direction of the substrate. One specimen from the sample grown at higher temperature was prepared so the electron beam entered along the [1$\bar{1}$0]-direction of the substrate. This is the specimen that was used for in-depth analysis with the JEOL ARM200F. The diffraction pattern from

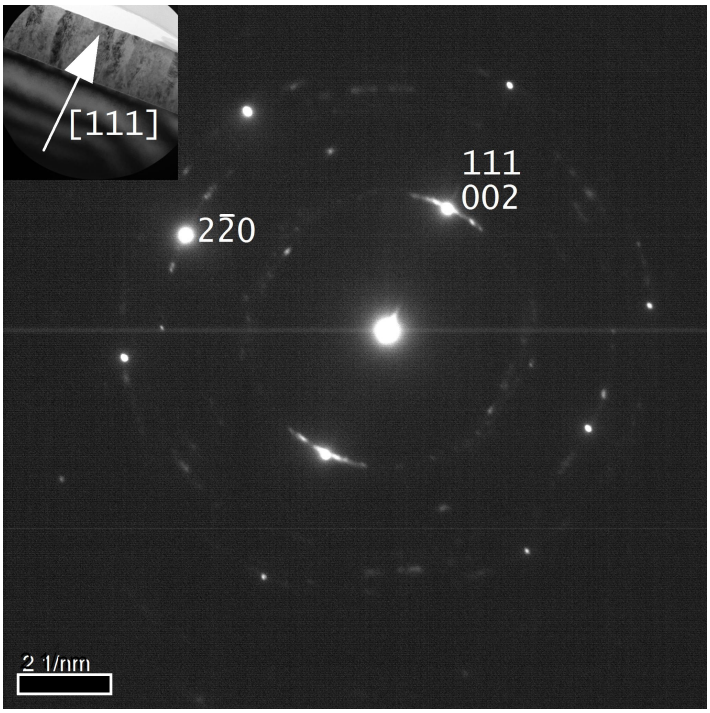

Figure 4.5: Diffraction pattern from the sample grown at lower temperature with the electron beam parallel to the [11$\bar{2}$]-direction of the substrate. The upper left corner shows the area used to obtain the diffraction pattern. The arrow indicates the [111]-direction of the substrate, which is also the growth direction. This pattern shows a polycrystalline wurtzite structure, textured in the [001]-direction, which is the same as the substrate's [111]-direction. Note that this is not representative of the low temperature sample. The wurtzite structure was only observed in one of the 15 areas that were studied.

this specimen is shown in Figure 4.6. This pattern shows that zinc blende is the dominant structure in the film, but weaker reflections are seen from wurtzite and from polytypes. All zinc blende reflections are mirrored across the (111)-axis with equal intensity, showing that the zinc blende structure appears as two mirrored structures with no apparent preferred orientation. All the structures are highly textured in the growth direction, which corresponds to [111] in zinc

blende and [001] in wurtzite. The reflections are slightly dragged out around the center spot, akin to the patterns seen in Figure 4.3 and Figure 4.4.

Figure 4.7 shows dark field images of two mirrored zinc blende reflections. Two areas corresponding to one reflection each can be distinguished, however there is no sharp twin boundary. Smaller bright areas can be seen inside the dark areas, indicating that the grains are not homogeneous.

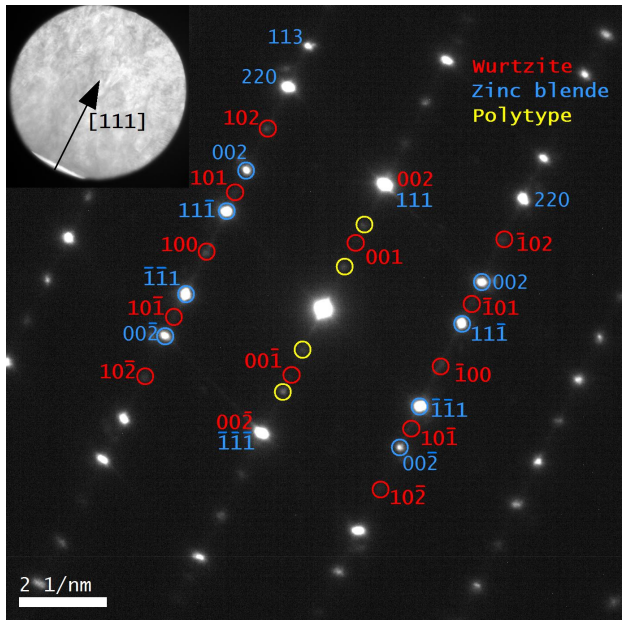

Figure 4.6: Diffraction pattern from the sample grown at higher temperature with the electron beam parallel to the $[1\bar{1}0]$-direction. The upper left corner shows the area used to obtain the diffraction pattern. The arrow indicates the [111]-direction in zinc blende, which is also the growth direction. The pattern shows that the dominant structure is zinc blende, and that it exists in two mirrored structures. All zinc blende reflections are mirrored across the (111)-axis, with no obvious preferred orientation. The pattern also shows weaker reflections from wurtzite as well as some extra reflections from polytypes. These different structures are all highly textured in the growth direction, which corresponds to [111] in zinc blende and [001] in wurtzite. As was the case in Figure 4.3 and Figure 4.4, the reflections are smeared out, slightly rotated around the center spot.

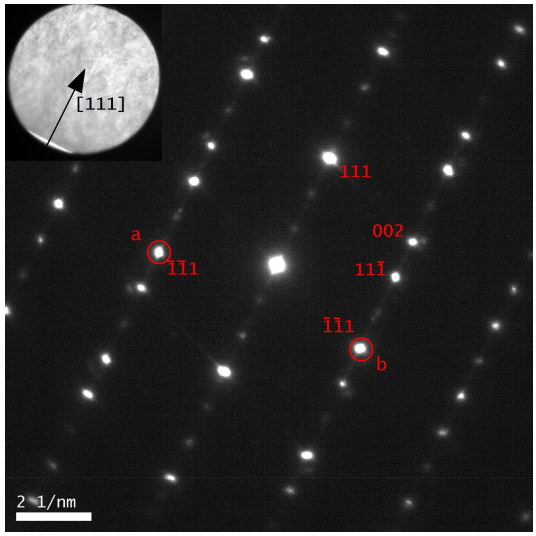

(a) The same diffraction pattern as is shown in Figure 4.6. Dark field image of the reflection marked with a can be seen in (b), and dark field of the reflection marked b can be seen in (c).

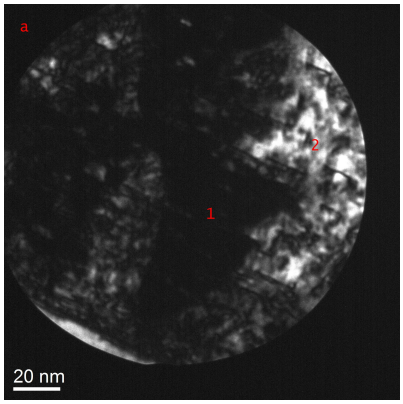

(b) Dark field of reflection a in Figure 4.7a

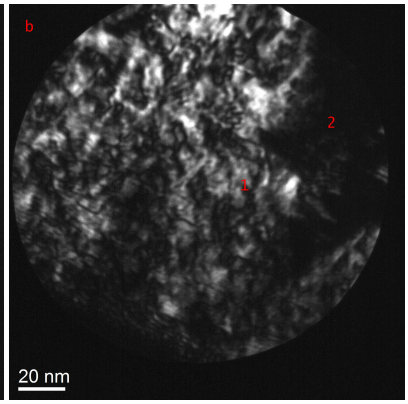

(c) Dark field of reflection b in Figure 4.7a

Figure 4.7: Image (a) shows the diffraction pattern from Figure 4.6 with two twin reflexes marked a and b. Dark field images of these reflections are shown in (b) and (c), respectively. Notice that the area marked 1 is dark in (b), and that area 2 is dark in (c). This indicates that these areas are predominantly made up of zinc blende, but the structures are mirror images of each other. Many small grains with different orientation can also be seen within the larger dark areas. These images were taken with the JEOL 2100.

4.2 Chromium content

The chromium content of the two samples grown at different temperature has been studied using EDS on the JEOL 2100. This was done by taking the average of ten scans at different locations in both films. The scans were done with the electron beam in the middle of the film, with a beam width of approximately 60% of the film thickness. The average atomic percentage of Zn, S and Cr is shown for the sample grown at lower temperature in Table 4.1, and for the sample grown at higher temperature in Table 4.2. The chromium content was found to be $4.00\% \pm 0.20\%$ in the sample grown at lower temperature, and $6.66\% \pm 1.00\%$ in the sample grown at higher temperature.

Table 4.1: Average chromium content in the sample grown at lower temperature.

	S [at.%]	Zn [at. %]	Cr [at. %]
average	53.51	42.48	4.00
σ	0.92	0.97	0.20

Table 4.2: Average chromium content in the sample grown at higher temperature.

	S [at.%]	Zn [at. %]	Cr [at. %]
average	54.79	38.55	6.66
σ	0.86	1.49	1.00

4.3 In-depth analysis

The sample grown at higher temperature was studied with a JEOL ARM200F operated by SINTEF researcher Per-Erik Vullum. This was done with high resolution imaging, EDS and EELS. The high resolution images were taken in TEM mode, EDS and EELS was done with maps(EDS only) and line scans in STEM mode. Unfortunately, the EELS scans did not get enough signal from sulfur for the software to analyze it. Since all results in this section comes from the same specimen made from the sample grown at higher temperature, this will not be specified in the text.

Crystal structure

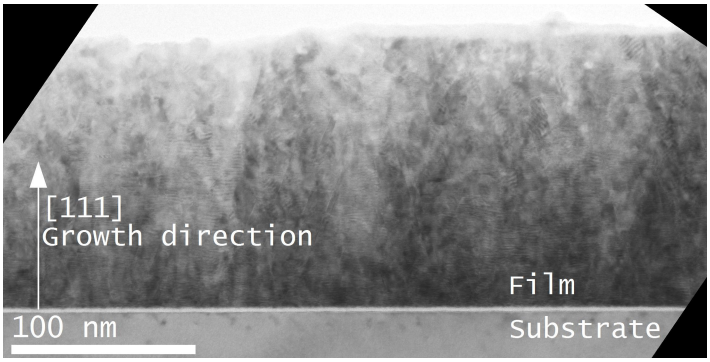

Figure 4.8: Bright field image of the sample grown at higher temperature. Moiré fringes from stacking faults can be seen throughout the film. There are trends in intensity along the growth direction, but no clear grains. An amorphous layer is seen at the substrate-film interface. Image taken with JEOL ARM200F.

A bright field image of the specimen can be seen in Figure 4.8. Trends in intensity can be seen in the growth direction, but no clear grains can be distinguished. Moiré fringes from stacking faults are observed throughout the film.

A high resolution image can be seen in Figure 4.9. The insets show FFT of

the area inside the white squares. Five different structures are seen. These are wurtzite, in (a); two different polytypes, in (b) and (c); and two mirrored zinc blends structures, in (d) and (e). The vast majority of the grains seen in high resolution images were longer in the direction of growth than in the direction parallel to the substrate-film interface. While doing FFT analysis, very small rotations were discovered between the grains. All the grains have a very high texture with growth along the [111]-direction of zinc blende or the [001]-direction of wurtzite. The orientational mismatch between the grains is typically less than 1-2 degrees. Because the grains are small, a small mask had to be used for FFT, causing the spots in the FFT to widen. This makes the small rotations hard to see in an image, because the spots of two overlaid FFTs would not be distinguishable. However, the small rotations were easy to see while doing live FFT from a mask when the mask was moved across the image.

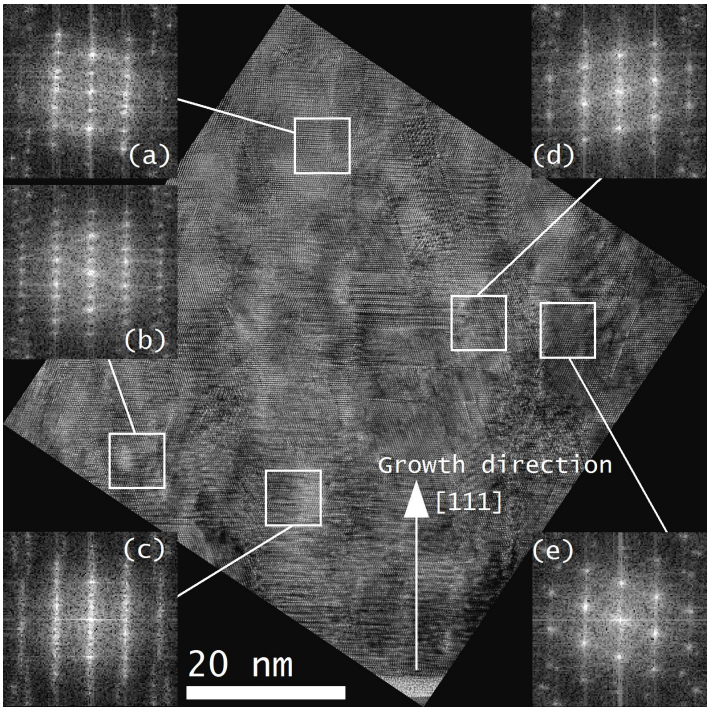

Figure 4.9: High resolution image of the sample grown at higher temperature. Substrate and an amorphous layer is visible at the bottom. The insets show FFT of the area inside the white squares. (a) shows wurtzite, (b) and (c) show two different polytypes and (d) and (e) show two mirrored zinc blende structures. The film consists of many small grains of these different structures. The grains are much longer in the direction of growth than in the direction parallel to the substrate-film interface. All the grains have a very high texture with growth along the [111]-direction of zinc blende or the [001]-direction of wurtzite. Image taken with JEOL ARM200F

EDS and EELS

EDS and EELS spectra were recorded for four line scans. Two were perpendicular to the substrate-film interface, and two were parallel to the interface. Of the two scans parallel to the interface, one was done close to the substrate and one was done closer to the edge of the film. The spectra from line scans presented here are all from different scans. This is to show that the same trends were present in all scans. An EDS map was also constructed. These scans and map were done to determine how Cr is distributed in the film.

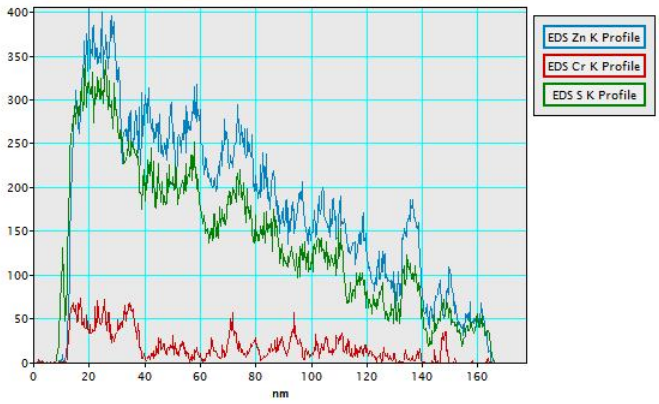

Figure 4.10: EDS line scan of the sample grown at higher temperature, scanning from the substrate to the edge of the film. The graph shows raw signal intensity as a function of distance, with the substrate being to the left and vacuum to the right. The film starts at approximately 15 nm. The overall decreasing signal strength is due to the specimen getting gradually thinner. The Cr signal shows that Cr is not evenly distributed in the film. A correlation is also seen between the Cr signal and the Zn signal. When the Cr signal increases, the Zn signal decreases and vice versa. A small S peak is also observed before the Zn or Cr signals appear. This is shown in greater detail in Figure 4.11

Figure 4.10 shows an EDS line scan done perpendicular to the substrate-film interface. The overall decreasing intensity is because the specimen is thicker close to the substrate, and gradually gets thinner further out in the film. The Cr

is not homogeneously distributed in the film. A correlation is seen between Cr and Zn. When the Cr signal increases, the Zn signal decreases, and vice versa. This correlation is not seen with Cr and S. A sharp S peak is seen before the Cr and Zn signals start. This is from the amorphous layer between the substrate and film. Figure 4.11 shows data from the same line scan as in Figure 4.10, but includes Si and O, and is zoomed in on the amorphous layer. This shows that the amorphous layer is an oxide layer, and that sulfur has diffused through the oxide layer during film growth.

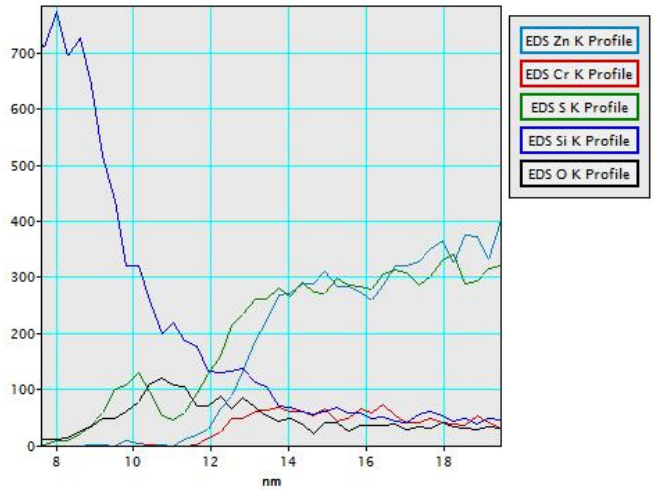

Figure 4.11: EDS line scan of the interface between the substrate and the film. The graph shows raw signal intensity as a function of distance, with the substrate being to the left and the film to the right. The S and O signals increase as the Si signal is decreasing. This shows that the amorphous layer between substrate and film observed in the high resolution images is an oxide layer and that S has diffused through the oxide layer during film growth.

Figure 4.12 shows an EDS line scan parallel to the substrate-film interface done close to the top of the film. As in Figure 4.10, the Cr is inhomogeneously distributed and an increase in Cr corresponds to a decrease in Zn.

Figure 4.13 shows an EELS spectrum from a line scan perpendicular to the

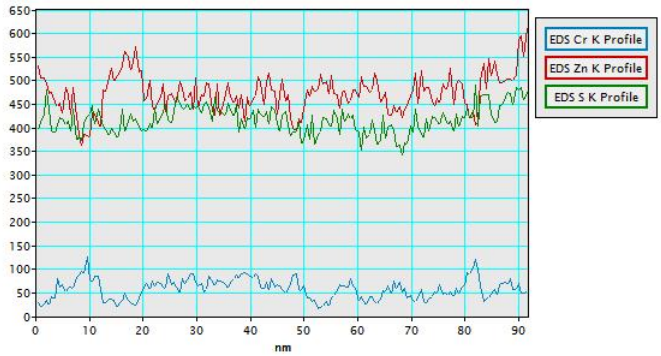

Figure 4.12: EDS line scan of the sample grown at higher temperature, scanning parallel to the substrate-film interface close to the top of the film. The graph shows raw signal intensity as a function of scanning distance. There is strong correlation between the Cr signal and the Zn signal. When the Cr signal increases, the Zn signal decreases, and vice versa.

substrate-film interface. The overall decreasing intensity is because the specimen is thicker close to the substrate, and gradually gets thinner further out in the film. The same is observed as in the EDS spectrum in Figure 4.10. The Cr is not homogeneously distributed in the film, and a correlation is seen between Cr and Zn. When the Cr signal increases, the Zn signal decreases, and vice versa. Note that this EELS scan is not from the same line scan as the EDS in Figure 4.10.

An EELS line scan parallel to the substrate-film interface, close to the substrate, can be seen in Figure 4.14. This scan shows the same effect as the other line scans. Cr is inhomogeneously distributed, and an increase in Cr corresponds to a decrease in Zn and vice versa.

EDS mapping was done for an area stretching from the substrate to approximately 12 nm out in the film. EDS signal from Cr, Zn, S, O and Si was recorded and mapped. These maps, along with a combined colour map and a STEM image of the area, is shown in Figure 4.15. The Cr map shows the inhomogeneous distribution of Cr. The diffusion of S as seen in Figure 4.11 is evident in the S

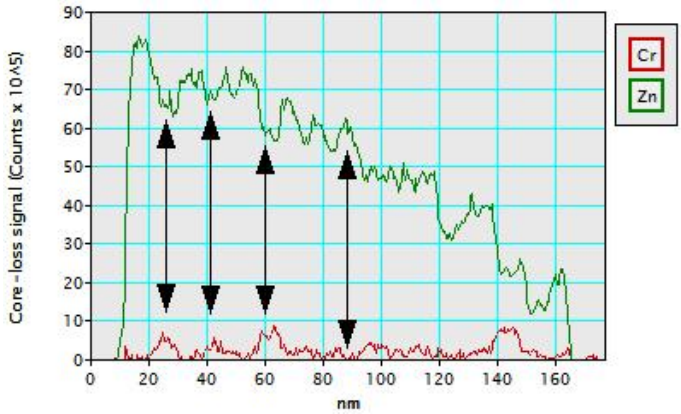

Figure 4.13: EELS line scan of the sample grown at higher temperature, scanning from the substrate to the edge of the film with substrate to the left and vacuum to the right. The graph shows raw signal intensity as a function of distance. The overall decreasing signal strength is caused by the specimen getting gradually thinner. A strong correlation is seen between Cr and Zn. When the Cr signal increases, the Zn signal decreases, and vice versa. The arrows are there to make this correlation easier to see. The varying signal from Cr indicates that it is not homogeneously distributed in the film.

map. In the colour map, Si is white, O is blue, S is red and Zn is green. Cr is not included because the intensity is too low for it to be visible.

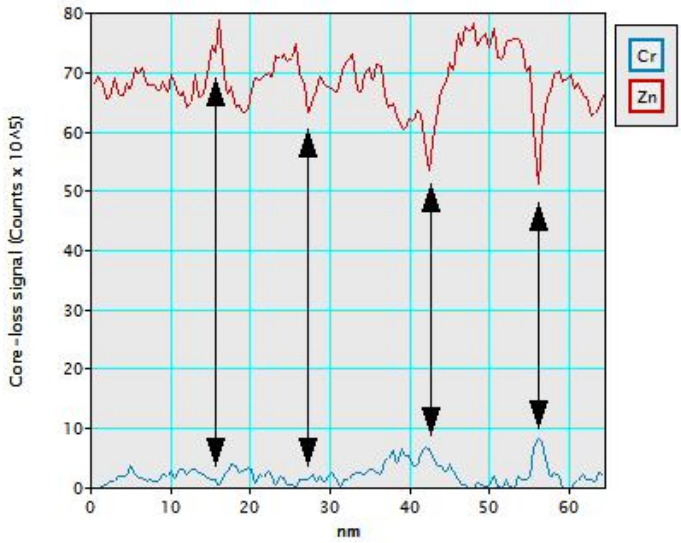

Figure 4.14: EELS line scan of the sample grown at higher temperature, scanning parallel to the substrate-film interface close to the substrate. The graph shows raw signal strength as a function of distance. A strong correlation is seen between Cr and Zn. When the Cr signal increases, the Zn signal decreases, and vice versa. The arrows are there to make this correlation easier to see. The varying signal from Cr indicates that it is not homogeneously distributed in the film.

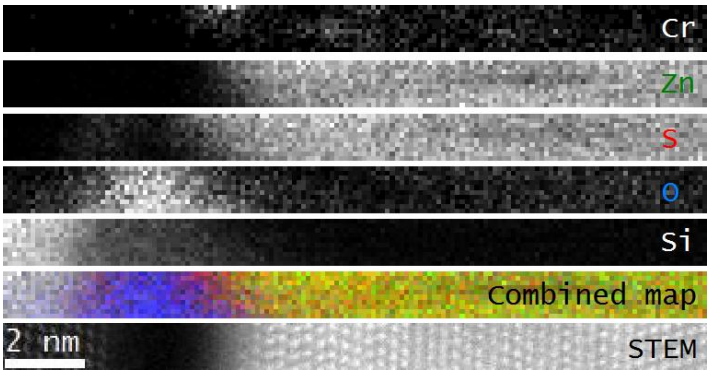

Figure 4.15: EDS map of the sample grown at higher temperature. All the EDS maps are from the area shown in the STEM image at the bottom. In order, from the top, they show: Cr intensity, Zn intensity, S intensity, O intensity, Si intensity, combined colour map, STEM image. In the combined map, Si is white, O is blue, S is red and Zn is green. Cr is not included in the combined map because the signal is too weak to be visible. The Cr map shows that Cr is not evenly distributed in the film. Both the S map and the combined map clearly show that S has diffused through the oxide layer. Note that the yellow colour is a mix of red and green from S and Zn.

Chapter 5

Discussion

5.1 Crystal structure

The diffraction patterns from the sample grown at a lower temperature, and the sample grown at a higher temperature, shown in Figure 4.3 and Figure 4.4 respectively, only show one diffraction pattern with no signs of a second structure. The only sign that these samples are not monocrystalline is the fact that the reflections are slightly dragged out, rotated around the center spot. This is seemingly in contradiction to what is observed in Figure 4.5 and Figure 4.6 which both clearly show wurtzite structure. However, the diffraction pattern in Figure 4.6 comes from a specimen which was prepared so the electron beam enters along the $[1\bar{1}0]$-direction of the substrate, while the specimen used in Figure 4.3 and Figure 4.4 have the electron beam along the $[11\bar{2}]$-direction of the substrate. These directions are perpendicular. The pattern from wurtzite in Figure 4.6, and Figure 4.5, show that the electron beam is parallel to the [100]-direction in wurtzite. The [100]-direction in wurtzite is perpendicular to the $[1\bar{1}0]$-direction. Diffraction patterns for zinc blende with the electron beam parallel to the $[11\bar{2}]$-direction and wurtzite with the beam parallel to the $[1\bar{1}0]$-direction simulated by

EMAPS [21] are shown in Figure 5.1. The patterns are virtually identical, and the d-value of the 111 reflection of zinc blende and the 002 reflection of wurtzite, as well as the $2\bar{2}0$ reflection of zinc blende and the $\bar{1}\bar{1}0$ reflection of wurtzite, only differ by 0.01 $Å^{-1}$ [14]. Thus the seemingly uniform structure of the film might very well be zinc blende patterns and wurtzite patterns overlapping. The twinning, which is apparent in Figure 4.6, is of course not noticeable in these patterns because they are symmetrical across the (111)-axis.

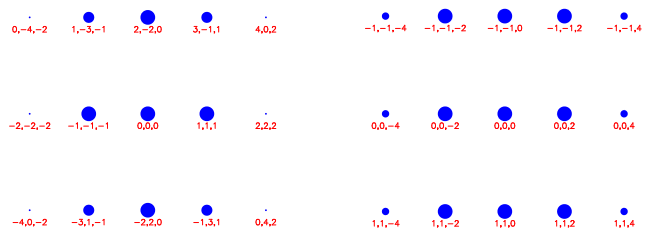

(a) Simulated diffraction image for zinc blende with electron beam parallel to the $[11\bar{2}]$-direction.

(b) Simulated diffraction image for wurtzite with electron beam parallel to the $[1\bar{1}0]$-direction.

Figure 5.1: Diffraction patterns simulated with EMAPS [21]. Figure 5.1a shows diffraction pattern for zinc blende with the electron beam parallel to the $[11\bar{2}]$-direction, and Figure 5.1b shows diffraction pattern for wurtzite with the electron beam parallel to the $[1\bar{1}0]$-direction. The patterns are virtually identical, showing that the seemingly single crystal structure shown in Figure 4.3 and Figure 4.4 could be a mix of zinc blende and wurtzite with overlapping diffraction patterns.

The high resolution images taken in the JEOL ARM200F, as shown in Figure 4.9, confirm that the dominant structure is zinc blende with a mix of wurtzite and two different polytypes. The high resolution images also show that the film consists of many very small grains. The grains are longer in the growth direction, which corresponds to [111] zinc blende or [001] wurtzite, but very short in

the direction parallel with the substrate-film interface. While doing FFT analysis, it was difficult do get only one kind of structure inside a 7 nm x 7 nm mask. The whole film is highly textured in the [111] zinc blende / [001] wurtzite direction, but with slight variations in the very small grains. The orientational mismatch between the grains is typically less than 1-2 degrees. This can explain the dragged out reflections which are observed in all the diffraction patterns from the films. The diffraction pattern from the sample grown at higher temperature in Figure 4.4 shows more dragged out reflections than the diffraction pattern from the sample grown at lower temperature in Figure 4.3, suggesting that there is less variation in the orientation of the grains in the sample grown at lower temperature.

The two different polytypes show rectangular diffraction patterns with the unit cell length along the hexagonal [001] direction being three times longer than wurtzite for the polytype in area (b) in Figure 4.9, and six times longer than wurtzite for the polytype in area (c) in Figure 4.9. This fits the H6 and H12 polytypes, which have both been observed in ZnS [3], but the resolution in the images was not good enough to investigate the stacking sequence.

5.2 Chromium distribution

The chromium content was found to be $4.00\% \pm 0.20\%$ in the sample grown at lower temperature, and $6.66\% \pm 1.00\%$ in the sample grown at higher temperature. Showing that growth at a higher temperature results in higher doping levels. The EDS and EELS scans show that there is chromium everywhere in the film, but that it is inhomogeneously distributed. They also show that there is strong correlation between chromium content and zinc content. Where there is more chromium, there is less zinc, and vice versa. This is in accordance with earlier studies [14].

Of special note is the amorphous layer between the substrate and the film. EDS scans clearly show that this is an oxide layer, and that sulfur has diffused through during film growth. The first part of the amorphous layer seems to be SiS. The thickness of this layer was fairly constant but varied from area to area between 1 nm and 4 nm.

5.3 Evaluation of sample preparation

Sample preparation is a very important part of any TEM work. All the specimen in this study were prepared with the cross-section dimpling and ion milling process explained in Section 3.2. The ion milling technique is good for creating thin samples, but it can also damage the sample as it can create an amorphous layer and it can cause thickness variations. During the semester this study was performed, a new ion milling system was installed in the sample preparation lab. Figure 5.2 shows two images of two specimen created from the same film sample, with the same sample preparation methods and the images are taken with the same electron microscope - JEOL 2100. The difference is that the specimen in Figure 5.2a was milled with the old PIPS, and the specimen in Figure 5.2b was milled with the new PIPS2. The contrast is a lot more even in Figure 5.2b, showing that the new PIPS2 causes a lot less damage to the specimen than the old PIPS. This is because the higher sputtering efficiency of the PIPS2 allows the last part of the milling to be done with lower ion energy.

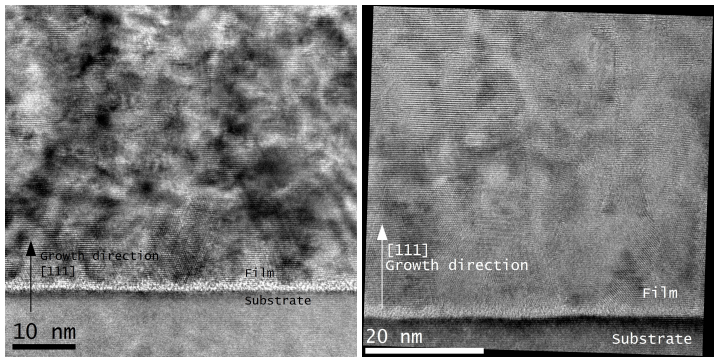

(a) PIPS1 (b) PIPS2

Figure 5.2: High resolution images from the same film sample, with the same sample preparation methods and the images are taken with the same electron microscope - JEOL 2100. The difference is that the specimen in Figure 5.2a was milled with the old PIPS, and the specimen in Figure 5.2b was milled with the new PIPS2. The contrast is a lot more even in image (b), showing that the new PIPS2 causes a lot less damage to the specimen than the old PIPS.

Chapter 6

Conclusion

Two Cr doped ZnS thin films grown at different temperatures were investigated by use of TEM. This was done to determine the crystallinity of the films and how the chromium was distributed in the films, to see if there was any difference between the two films.

High resolution images show stacking faults throughout both films. Diffraction images from both samples show very high texture along the growth direction, which corresponds to [111]-direction in zinc blende or [001] in wurtzite. The diffraction pattern for both samples are dragged out, slightly rotated around the center spot. This effect is grater in the sample grown at higher temperature. High resolution images of the sample grown at higher temperature show that this rotation is caused by many very small grains with slight deviations in orientation, typically less than 1-2 degrees. FFT analysis of the high resolution images also show that the sample consists of predominantly zinc blende, with a mix of wurtzite and two different polytypes.

EDS and EELS scans of the sample grown at higher temperature show that there is chromium throughout the film, but that it is inhomogeneously distributed. A strong correlation is seen between chromium content and zinc content. Ar-

eas with higher chromium concentration has lower zinc concentration and vice versa.

The chromium content for the two samples was studied with EDS analysis. It was found to be $4.00\% \pm 0.20\%$ in the sample grown at lower temperature, and $6.66\% \pm 1.00\%$ in the sample grown at higher temperature.

An amorphous layer was observed between the substrate and the film. This was determined to be an oxide layer, and EDS scans revealed that sulfur has diffused through the layer to form SiS.

Chapter 7

Further work

One of the main limitations of TEM is that one can only study a very small area at a time. It is always advisable to study more samples to get more statistically significant results, and to rule out localized phenomena. In-depth studies should be done for both film samples to have directly comparable results. The amorphous oxide layer observed between the substrate and the film in these film samples should be avoided. Such an oxide layer will severely reduce the efficiency of any solar cells, and could very well be affecting the film growth. Getting images with higher resolution to determine what polytypes the film consists of could be done, however the value of such a study might be questionable since zinc blende is the desired structure for solar cells applications.

It is important for anyone continuing this work to prepare the samples so the electron beam enters along the $[1\bar{1}0]$-direction of the zinc blende structure. This is necessary to separate zinc blende from wurtzite.

Bibliography

[1] National Aeronautics and Space Administration (NASA). A blanket around the earth. http://climate.nasa.gov/causes/. Accessed: 16.12.2014, 2014.

[2] National Aeronautics and Space Administration (NASA). The current and future consequences of global change. http://climate.nasa.gov/effects/. Accessed: 16.12.2014, 2014.

[3] Mizuhiko Akizuki. Investigation of phase transition of natural zns minerals by high resolution electron microscopy. *American Mineralogist*, 66:1006–1012, 1981.

[4] F. Boutaiba, A. Belabbes, M. Ferhat, and F. Bechstedt. Polytypism in zns, znse, and znte: First-principles study. *Physical Review B*, 89, 2014.

[5] A. D. Dinsmore, D. S. Hsu, S. B. Qadri, J. O. Cross, T. A. Kennedy, H. F. Gray, and B. R. Ratna. Structure and luminescence of annealed nanoparticles of zns:mn. *Journal of Applied Physics*, 88(4985), 2000.

[6] M. Iqbal. *An Introduction to Solar Radiation*. Academic Press, 1983.

[7] Charles Kittel. *Introduction to Solid State Physics*. John Wiley & Sons, Inc., eighth edition, 2005.

[8] A. Luque and A. Martí. Increasing the eciency of ideal solar cells by photon induced transitions at intermediate levels. *Physical Review Letters*, 78(26):5014–5017, 1997.

[9] A. Luque and A. Martí. The intermediate solar cell: Progress toward the realization of an attractive concept. *Advanced Materials*, 22(2):160–174, 2010.

[10] A. Luque, A. Martí, and C. Stanley. Understanding intermediate-band solar cells. *Nature Photonics*, 6(3):146–152, 2012.

[11] Oliver Morton. Solar energy: A new day dawning?: Silicon valley sunrise. *Nature*, 443(7107):19–22, 09 2006.

[12] Jenny Nelson. *The Physics of Solar Cells*. Imperial college press, 2013.

[13] Naomi Oreskes. The scientific consensus on climate change. *Science*, 306(5702):1686, December 2004.

[14] Eivind Seim. Tem characterization of cr-doped zns thin films for solar cell applications. Master's thesis, Norwegian University of Science and Technology(NTNU), 2014.

[15] William Shockley and Hans J. Queisser. Detailed balance limit of efficiency of p-n junction solar cells. *Journal of Applied Physics*, 32:510–519, March 1961.

[16] L. Soonchindt, D. Etienne, and et al. J.P. Marchand. The composition and temperature dependencies of the fundamental bandgap in znsxse1-x alloys. *Surface Science*, 0(378):383–1979, 86.

[17] Ben G. Streetman and Sanjay Kumar Banerjee. *Solid State Electronic Devices*. Pearson, sixth edition, 2006.

[18] Downs R T. The rruff project: an integrated study of the chemistry, crystallography, raman and infrared spectroscopy of minerals. Program and Abstracts of the 19th General Meeting of the International Mineralogical Association in Kobe, Japan. O03-13, 2006.

[19] Katsuaki Tanabe, Denis Guimard, Damien Bordel, and Yasuhiko Arakawa. High-efficiency inas/gaas quantum dot solar cells by metalorganic chemical vapor deposition. *Applied Physics Letters*, 100(19), 2012.

[20] David B. Williams and C. Barry Carter. *Transmission Electron Microscopy Part 1: Basics*. Springer Science+Business Media, LLC 1996, 2009.

[21] J.M. Zuo and J.C. Mabon. Web-based electron microscopy application software: Web-emaps. Microsc Microanal 10(Suppl 2), 2004; URL: http://emaps.mrl.uiuc.edu/.